Direct measurement of residual strains in CFRP-tungsten hybrids using embedded strain gauges

Kanerva, M[a,*], Antunes, P[b,c], Sarlin, E[a], Orell, O[a], Jokinen, J[a], Wallin, M[d], Brander, T[d], Vuorinen, J[a]

[a] *Tampere University of Technology, Department of Materials Science, P.O.B 589, FI-33101 Tampere, Finland*
[b] *Instituto de Telecomunicações - Aveiro, P.O.B 3810-193, Aveiro, Portugal*
[c] *Physics Department and I3N, Aveiro University, Campus de Santiago, P.O.B 3810-193, Aveiro, Portugal*
[d] *Aalto University, School of Engineering, Department of Mechanical Engineering, P.O.B 14300, FI-00076 Aalto, Finland*

Abstract

In this work, the implementation of fully embedded electrical resistance strain gauges was studied for a hybrid material system. The samples were laminated using carbon-fiber reinforced plastic (CFRP) and tungsten. The raw materials and the adhesive used for bonding strain sensors were characterized to understand the overlapping sources of non-linearity and error. Test-specific correction functions for thermal output were determined for strain gauge measurement and comparative fiber Bragg grating (FBG) measurement. The strain accumulation in the fiber direction during the cool-down phase of different cure cycles was analyzed using a finite element simulation. According to the results, embedded electrical resistance strain gauges can be used to determine thermal expansion of a hybrid laminate at an acceptable accuracy when thermal output is compensated using case-specific correction functions accounting for measurement setup, stiffness of the gauge bonding adhesive, and embedding.

Keywords: Strain measuring, Hybrid laminate, Residual stress, CFRP

*Corresponding author. Tel:+358-40-718 8819
Email address: Mikko.Kanerva@tut.fi (Kanerva, M)

1. Introduction

Residual stresses are inevitable in multimaterial systems when continuous strain distributions prevail between material components with different thermal or hygroscopic expansion coefficients [1, 2]. Residual stresses can lead to warping, loss of mechanical properties and premature debonding in adhesive joints [3], laminated composite structures [4], and large 3-D printed parts [5]. Ultimately, local residual strains can exceed the yield or first failure strain limit of material.

Simulations of residual stresses for systems of isotropic materials on different length-scales have been published extensively (e.g. [6, 7]). Models of thermal strains in composite and hybrid systems can be found as well [8, 9]. Realistic simulation of crack onset and delamination growth in metal-composite hybrids require verified data of residual strains to compute the elastic strain energy stored in the structure prior to external, mechanical loading [10]. However, it is well known that exact thermal expansion coefficients for hybrid materials are difficult to acquire [11].

Residual stresses in structures are determined experimentally by first measuring strains. Residual strains have been measured successfully in composites using fiber Bragg grating (FBG) sensors embedded between the (prepreg) layers during the lay-up of the composite. FBG can be used to measure matrix shrinkage strain [12], to monitor laminate curing process in-situ [13], and to determine strains based on the transverse stress effect [14]. Additionally, optical fibers with FBG sensors are advantageous in multiplexing techniques, e.g. for quasi-distributed structural monitoring [15, 16]. However, optical fibers are mechanically weak, e.g. compared to electrical resistance strain gauges, and care must be taken to place them within the lay-up [17] and thread out the fiber ends from the composite structure [18]. Also, apparent thermal output of FBG sensors (false strain indication) cannot be greatly adjusted [15], which means that the determined residual strain is prone to errors due to assumed bonding of the sensor to the matrix polymer or laminate surface at high temperatures. In turn, foil strain gauges are relatively adjustable and mechanically robust yet their strain indication is sensitive to numerous error sources [19]; by applying appropriate error compensation, thermal expansion of composite materials can be determined [20]. However, especially for carbon-fiber-reinforced composites with negative thermal expansion coefficient, the correct absolute value of residual strain per laminate cure cycle is difficult to obtain via embedded strain gauge placement [21].

Technically, the smallest measurable strain for FBG and strain gauge systems is limited only by the noise or drift due to signal amplification and faulty connectors.

Other direct methods for residual strain measurements exist, e.g. methods based on surface strains and metal crystal structure, though the output tends to be scattered [22, 23]. Several indirect methods for determining residual strains exist, i.e. the strain distributions are calculated based on measurements of a secondary quantity. Typically, the deformations of a structure are measured along the free surfaces, e.g. using a length scale, profilometer or material tester [24, 25, 26]. Even in the case of strain gauges or FBG sensors attached on free surfaces, the internal stress state must be computed using a suitable model of the material system in question.

In conclusion, the determination of residual strains in composite or metal-composite hybrid structures with embedded sensors is evidently more important and challenging where higher is the stiffness and weaker are the interfaces between the constituent materials. In this study, we focus our efforts on residual strains in a satellite enclosure material where carbon-fiber-reinforced plastic (CFRP) is laminated with tungsten (W) foils [27]. Due to the very high stiffness of the constituent materials, the deformations due to thermal loads are small and the stresses are high. We analyze the application of strain gauges for measuring internal residual strains directly by embedding the gauges into the hybrid structure. We apply typical cure cycles recommended by the manufacturer for a modern out-of-autoclave process. Correction functions are determined for a robust strain measurement system. The strain gauge measurement results are compared with measurements using FBG sensors, laser profilometry and a finite element simulation.

2. Materials and Methods

2.1. Epoxy samples for 3-point bending

Three-point bending samples were prepared to study the behavior of the epoxy resin that was used later for bonding strain gauges and optical fibers on samples. The resin was a room-temperature-curing epoxy resin (Araldite LY 5052, Aradur 5052 hardener, Huntsman International) mixed using a hardener-resin ratio of 38% (weight/weight). A mould (20 cm $\times$ 20 cm) was filled with the resin up to nominal 6 mm thickness and cured at ambient conditions. Samples were cut to dimensions (15 mm $\times$ 80 mm $\times$ 6 mm)

($l \times w \times t$) using a circular saw. Before the testing, the samples were post-cured and dried in a vacuum oven for three days (50 ℃, $5{\cdot}10^4$ Pa vacuum pressure).

2.2. Tungsten samples

Tungsten was acquired in a rolled foil form (99.95% purity, 50 µm thickness, Alfa Aesar GmbH). Samples of two different sizes were cut to account for possible 3-D effects (19 mm × 70 mm & 19 mm × 38 mm). Both sizes were used for calibrating the strain gauge and optical fiber measurements by studying the measured thermal expansion. Additionally, the latter was used for preparing CFRP-tungsten hybrid samples.

2.3. Carbon-fiber-reinforced plastic (CFRP) samples

CFRP was prepared using a pre-preg tape (areal weight of 300 g/m^2, Advanced Composites Group, Umeco) consisting of MTM 57 epoxy-based resin (32% (weight/weight), ACG, UK) and unidirectional (UD) M40J(12K) carbon-fibers (Toray, USA). The nominal thickness of a pre-preg layer was 0.29 mm. The pre-preg was used for preparing two different types of samples: Firstly, thermal expansion of fully cured CFRP was studied using a UD laminate sample with final sample dimensions of 41 mm × 20 mm × 8 mm and a lay-up of $[0_{30}]$. The laminate was built on an aluminium mould, covered by a vacuum bag and cured using a traditional autoclave (ramp 1.1 ℃/min, 1 h dwell at 120 ℃, $8{\cdot}10^4$ Pa vacuum pressure). A layer of release film against the mould and a peel ply layer on top of the laminate was stacked under the vacuum bag. The sample was cut into shape using a circular diamond saw and a grinding machine.

Secondly, the interaction between curing CFRP pre-preg and embedded strain sensors was studied using a UD laminate sample with final dimensions of 39 mm × 19 mm × 6.25 mm and a lay-up of $[0_{10}/S/0/S/0_{10}]$ where 'S' refers to a sensor (FBG sensor / strain gauge). The laminate was built in a silicone mould (see Section 2.6) where the mould with the laminate was vacuum bagged and cured in an air-circulating oven (cure cycle in Fig. 1). Two layers of peel ply fabric were placed between the laminate and the silicone mould cover.

2.4. CFRP-tungsten hybrid samples

Residual strains and thermal expansion were studied for CFRP-tungsten hybrid material. Laminates consisted of CFRP and tungsten (W) layers

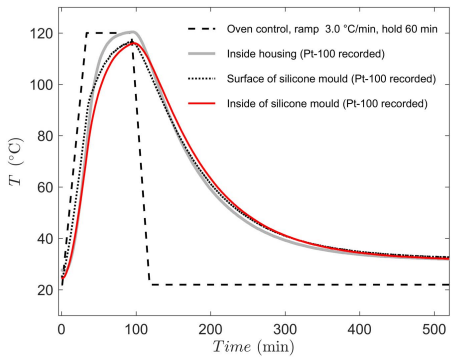

Figure 1: The cure cycle used for preparing CFRP and studying CFRP-W hybrid samples.

defined above and were stacked, using a lay-up of $[0_{14}/W/0_7]$, into a silicone mould (see Section 2.6). The tungsten layers were degreased using acetone before the bonding of a sensor. The final dimensions of the samples were 38 mm × 19 mm and the nominal thickness was 6 mm. The laminate and the mould was vacuum bagged and the curing was controlled using an air-circulating, digitally controlled oven (see Fig. 1 for cure cycle). Two layers of peel ply fabric were placed between the laminate and the silicone mould cover. For the samples with sensors, a configuration of $[0_{14}/W/S/0_7]$ was used ('S' refers to an FBG sensor and strain gauge).

2.5. Test setup for 3-point bending

The 3-point bending tests were performed using a testing machine (Electropuls E 3000, Instron) with a 3 kN load cell, 3-point bend test setup and an air-circulating chamber. The tests were performed in ambient laboratory conditions and also at 90 ℃; load head displacement-rate of 2 mm/min was used. The samples for the elevated temperature testing were kept inside the oven for a minimum of 15 minutes prior to testing to let temperature stabilise inside the samples. A pre-force of -15 N was applied prior to actual test start. Force-deflection data was acquired for making comparisons of flexural strength and stiffness at different test conditions. The flexural moduli were calculated over the linear range using least squares fitting. Five samples per temperature were tested.

2.6. Test setup for sensor calibration and residual stress measurements

The sensor calibration with the tungsten foil samples and studies of CFRP thermal expansion were performed using a housing with a balsa core and

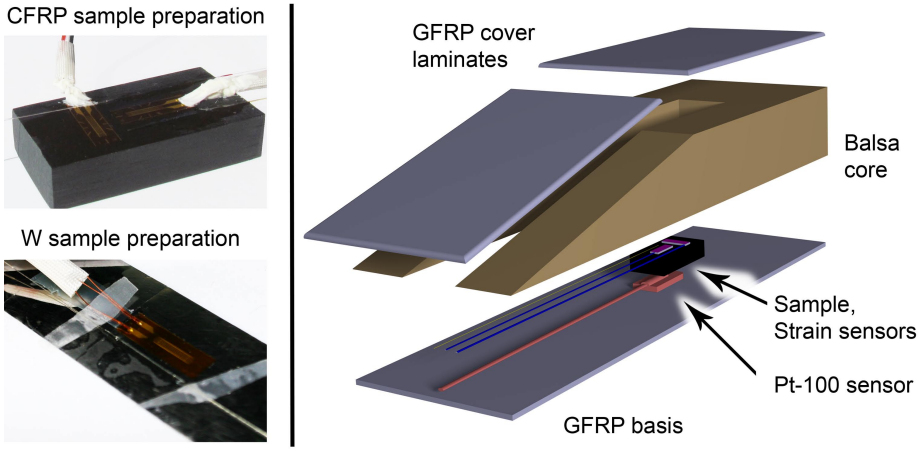

Figure 2: Sample preparation and the schematic of the test setup and housing used for sensor calibration.

glass-fiber-reinforced plastic covers (see Fig. 2) and the entire setup was packed inside a vacuum bag. The housing allowed free as possible expansion of the sample materials in vacuum conditions. For the studies of residual strains in the CFRP-tungsten samples, a silicone mould with two sample slots was used, as illustrated in Fig. 3. To avoid breakage of the optical fibers due to pressing by the vacuum bag, two CFRP plates were mounted and held at the edge (15 mm) of the mould, to form a smooth exit out of the silicone mould for the fibers. Local temperature inside the mould and housing were monitored and recorded synchronously (Signasoft 6000, Peekel Instruments, NL) with strain measurements. For the temperature measurements, Pt-100 sensors (RTF4-2, Labfacility, UK) were placed inside the housing and mould and also outside the vacuum bag, fixed on top of the housing. Vacuum condition (pressure difference) of $4 \pm 2 \cdot 10^4$ Pa was used for all the tests. A minimum of five cycles per sample type were measured. The influence of vacuum and the silicone mould on measurement data was studied via supplementary testing.

2.7. Strain gauges

Strain measurements were carried out using high-temperature resistant, three-wire strain gauges (KFRP-5-120-C1-1, Kyowa Electronic Instruments). These gauges have a polyimide gauge base and operation temperature range of -196–200 ℃. The gauges had an adoptable coefficient of thermal expansion

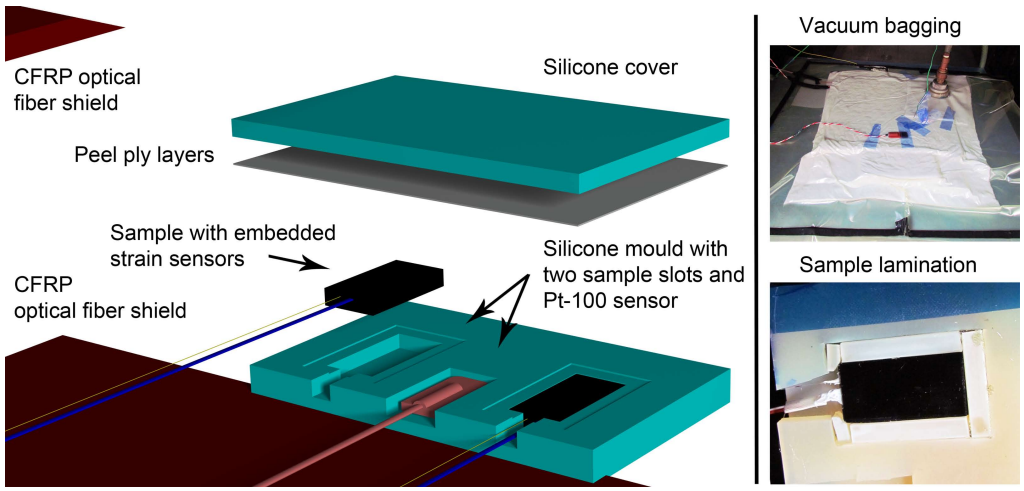

Figure 3: Sample lamination and the schematic of the test setup and mould used for residual strain measurements.

(CTE) of 1.0 µm/(m℃) according to the manufacturer. The gauges were attached to the raw material samples using the epoxy resin defined above (see Section 2.1) to form a strong bond with the tungsten foil surface. The bonding epoxy was first let to cure in ambient laboratory conditions, which after the bond was post-cured (tungsten and CFRP samples) or laminated into a CFRP-tungsten hybrid. The resistance changes in the gauges were monitored and recorded using a multipoint amplifier (Peekel Instruments, NL) and the manufacturer's analysis software (Signasoft 6000). Gauges were connected via (recorded) quarter-bridge connection. The three-wire connection was used to minimize the false strain indication due to the resistance change in the lead wires [28].

The gauge manufacturer offers several fitted correction factors for the different thermal effects in a generalized case. However, in this study, it was needed to accurately observe the strain caused by the CTE mismatch in the hybrid material samples. Due to the robust test setup and need for measuring the effective expansion (i.e. no need to distinguish between cure shrinkage, thermal expansion and hygroscopic strains), a test setup-specific correction function, $Cr(T)$, was defined here:

$$\varepsilon_{corrected}(T) = \varepsilon_{RD}(T) + Cr(T), \tag{1}$$

where

$$Cr(T) = -\left[\varepsilon_{RD,c}(T) - \alpha_{m,c}(T - T_0)\right], \tag{2}$$

and $\varepsilon_{RD,c}$ is the raw data from a calibration test, T_0 is the ambient (initial & final) temperature of the calibration cycle, and $\alpha_{m,c}$ is the first (linear) coefficient of thermal expansion of the calibration material. The correction function for the strain gauges was determined using the pure tungsten foil as a calibration sample (see Section 2.2) and a regression was applied to the cool-down phase. The fundamental background of the strain gauge error sources is given in Appendix A.1.

2.8. Fiber Bragg grating (FBG) sensors

Comparative strain measurements were carried out using optical fibers with FBG sensors. The acquisition system was a W3/1050 Series Fiber Bragg Grating Interrogator (Smart Fibers Ltd) with a wave-length range of 1510–1590 nm. The interrogator was operated using a Remote Interface W3 WDM (version 1.04) and all the fibers with the FBGs were individually tailored by Instituto de Telecomunicações (Aveiro, Portugal).

In this study, a thermal-strain compensation sensor (collocating sensor) was located in each fiber 20 mm apart from the actual measuring sensor bonded to the sample. The measuring sensor was either embedded inside the sample material (i.e. CFRP) or adhesively bonded using the epoxy resin defined above (see Section 2.1). Due to the fact that the compensation sensor does not experience exactly the same temperature as the measuring sensor, and also due to the epoxy bonding, an additional correction function was determined as defined by Equation 1. The correction function for the FBG sensors in this study was determined using the pure tungsten foil as a calibration sample (see Section 2.2). The fundamental background of the thermal compensation using a collocating sensor is given in Appendix A.2.

2.9. Profilometry

Due to the anisotropic thermal expansion of CFRP and also due to the asymmetric lay-up, the CFRP-tungsten samples bend during a cure cycle. Overall surface shape on a CFRP sample was measured using 3-D optical profilometer (InfiniteFocus G5, Alicona); the surfaces were analyzed without any preparation at a ×5 magnification and 0.4–3.5 µm resolution. Local measurements on hybrid samples were performed using a laser profilometer (Wyko NT1100, Veeco); a region of 5 mm × 4 mm was measured and the radiuses of curvature were determined in the lateral and longitudinal direction using least squares fitting. Prior to local measurements, a thin layer of gold was sputtered over each sample surface to enhance reflectivity.

2.10. Scanning electron microscopy (SEM)

A field emission gun scanning electron microscope (ULTRAplus, Zeiss) was used for studying the bonded sensors. Cross-sectional microscopy samples were extracted from the CFRP-tungsten hybrids using a diamond saw, embedded in a moulding glue, polished and gold-coated prior to imaging.

2.11. Thermo-mechanical analysis

The thermo-mechanical properties, i.e. glass transition temperature, T_g, and the exotherm during curing, were studied for the bonding epoxy, pre-preg and fully cured CFRP. Dynamic mechanical thermal analysis (DMTA) was performed for UD CFRP samples (1.84 mm $\times$ 4 mm $\times$ 40 mm) in the fiber direction using a Pyris Diamond DMA (PerkinElmer) at 1 Hz frequency in a single cantilever mode. The curing and development of T_g were analyzed for the bonding epoxy after curing in ambient laboratory conditions and for the CFRP pre-preg (in β-stage) using a DSC 204 F1 (Netzsch) dynamic scanning calorimeter (DSC). Four samples per analysis were applied for CFRP and two samples for the bonding epoxy.

2.12. Finite element analysis (FEA)

The residual strain distribution in the CFRP-tungsten hybrid was simulated using a finite element code Abaqus/Standard 6.14-2 (Simulia, Dassault Systèmes). The three-dimensional CFRP geometries were meshed using linear hexahedrons with enhanced bending behaviour (C3D8I) and the tungsten layer using quadratic full-integrated elements (C3D20). The materials were presumed to behave in a linear-elastic manner throughout the simulated temperature range; the input material properties of tungsten and CFRP are given in Table 1. The interface between the CFRP parts and the tungsten layer was modelled using cohesive elements (COH3D8) to allow natural interface response. The cohesive law parameters were fitted based on 3-point bend testing, and power laws were used to define damage onset and full nodal release, as reported in our previous study [29]. The input parameter values are given in Table 2. As a boundary condition, only the free-body motion was prevented by applying zero translation to X, Y and Z-direction for a single element in one end of the model. Thermal loading of ΔT = -98 ℃ was applied over the model to simulate residual strains due to the cool-down phase of the real sample manufacture. The model and the applied coordinate system are shown in Fig. 4.

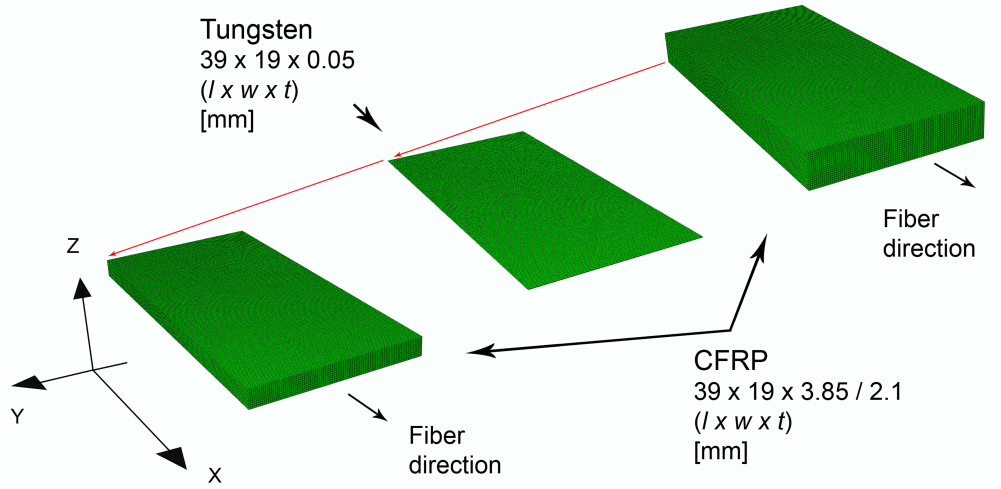

Figure 4: Finite element model and the applied coordinate system in this study.

Table 1: Young's moduli and shear moduli, E, Poisson's ratios, ν, and coefficients of thermal expansion, CTE, used for the finite element modelling of the hybrid sample. The coordinate system for material directions is given in Fig 4.

Engineering constant (unit)	CFRP [27]	Tungsten [30]
E_{xx} (GPa)	191.5	410
E_{yy}, E_{zz} (GPa)	6.3	410
E_{xy}, E_{yz}, E_{xz} (GPa)	7.2	(160.2)
$\nu_{xy}, \nu_{yz}, \nu_{xz}$ (-)	0.31[b]	0.28
CTE_{xx} (10^{-6} 1/°C)	-0.952[a]	4.5
CTE_{yy}, CTE_{zz} (10^{-6} 1/°C)	43.85[a]	4.5

[a] Value based on testing, see Section 3.3

[b] ν_{xz} approximated based on ν_{xy}

Table 2: Properties of the cohesive zone modelling. Directions 1, 2 and 3 refer to opening, shearing and twisting crack tip opening. [29]

Parameter (unit)	value [29]
Cohesive stiffness, K (N/m^3)	$1 \cdot 10^{15}$
Cohesive strength, τ_1, τ_2, τ_3 (MPa)	95, 95, 95
Critical strain energy release rates, $G_{Ic}, G_{IIc}, G_{IIIc}$ (J/m^2)	40, 40, 10 000

3. Results and Discussions

3.1. Polymer characterization

Typical DSC results for the bonding epoxy are shown in Fig. 5(a). Though the epoxy system had cured readily at ambient conditions, the curing clearly continued during the first DSC cycle (3 ℃/min, till 200 ℃). Based on the second DSC cycle, the glass transition was observed to occur over a wide temperature range and the mid-point was determined: $T_g = 116.9 \pm 2.2$ ℃. Typical DSC results for the CFRP pre-preg are shown in Fig. 5(b) and it can be seen that the cure reactions (exotherm) begin after reaching 114–115 ℃ (ramp 3 ℃/min). As it is typical for epoxy-based matrices, the glass transition was observed to occur over a wide temperature range and the mid-point was determined: $T_g = 126.0 \pm 1.1$ ℃ (second cycle, ramp 3 ℃/min). Typical DMTA results for the fully cured UD CFRP are shown in Fig. 5(c). Based on DMTA, the extrapolated glass transition onset according to storage modulus was 114.4 ± 0.86 ℃ and tanδ peak occurred at 132.7 ± 0.36 ℃. The results correspond well to the T_g values reported by the manufacturers, 116–120 ℃ (onset) [31] and 125 ℃ [32] for the bonding epoxy and CFRP in fully cured condition, respectively.

The 3-point bend testing results for the bonding epoxy at the ambient laboratory conditions and 90 ℃ are shown in Fig. 5(d). At a room temperature, the behavior of the epoxy samples was brittle and the ultimate flexural strength was determined to be 118.4 ± 9.5 MPa. At 90 ℃, the flexural modulus decreased by 37% and nonlinearity strain by 18%. Based on the flexural tests, the softening of the bonding epoxy had clearly onset at 90 ℃.

3.2. Correction functions Cr(T)

Strain gauge and FBG sensor data were corrected using tungsten as a calibration material. Thermo-mechanical properties of tungsten are well reported in the current literature and the CTE of rolled pure tungsten foil has been determined to be 4.5 µm/(m ℃) [30] over the temperature range applied to this study. Raw data from FBG sensors is shown in Fig. 6(a) and it can be seen that the slope of the strain-temperature (ε-T) curve upon the heating is non-linear due to the slower heat-up in the Pt-100 sensor compared to the tungsten foil sample. For every first cycle per sample, the bonding of the FBG fiber relaxes significantly. However, due to the post-curing of the bonding epoxy, the behavior is essentially linear during the cool-down phase and subsequent cycles.

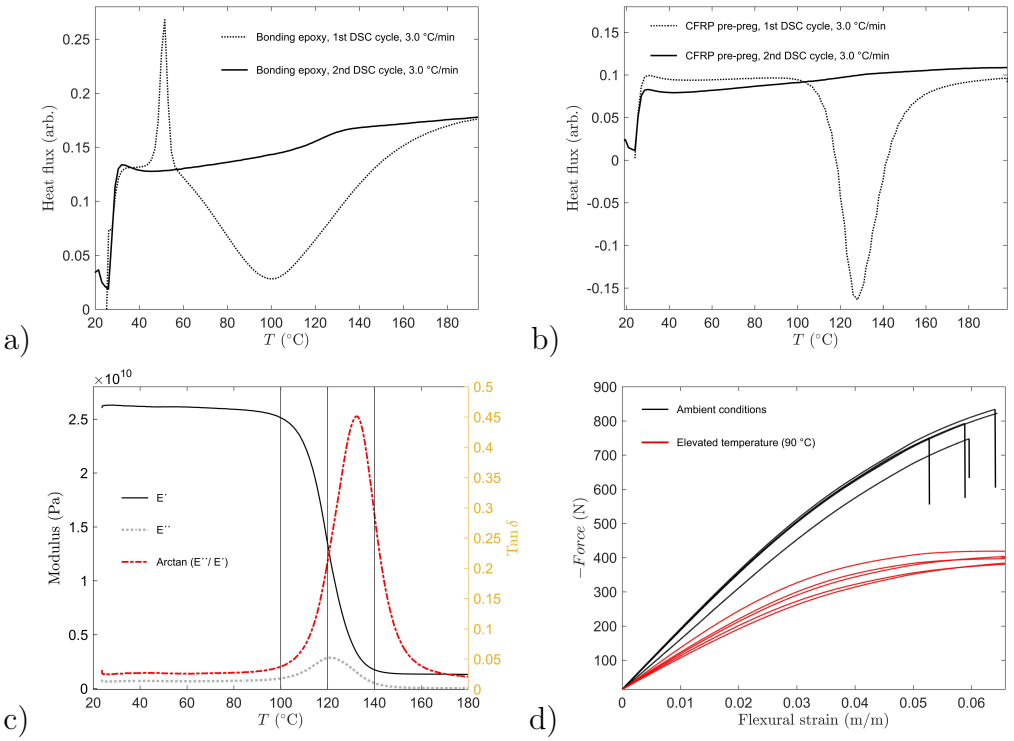

Figure 5: Thermo-mechanical analysis for the polymers used: a) typical DSC curves for the bonding epoxy after room temperature cure; b) typical DSC curves for the CFRP pre-preg; c) typical DMA curves for fully cured CFRP used in this study; d) 3-point bending test results.

The FBG sensor data after subtraction of strain data of the compensation sensor (i.e. temperature compensation) is shown in Fig. 6(b). The temperature compensation clearly extracts part of the initial non-linearity, yet the slope does not fully correspond to tungsten CTE due to slightly added expansion by the bonding epoxy. By least squares fitting a line for the cool-down phase below the glass transition (relaxation) of the bonding epoxy ($T = 114 \pm 3$ ℃...37 ± 3 ℃), an apparent CTE of 4.806 ± 0.180 µm/(m ℃) was determined. Based on the known CTE of tungsten [30], linear correction functions $Cr(T)$ = -0.106 µm/(m ℃) $(T - T_0)$ and $Cr(T)$ = -0.357 µm/(m ℃) $(T - T_0)$ were determined for every first cycle after sensor bonding and further cycles, respectively.

Raw data from strain gauges is shown in Fig. 6(c). Strain gauge measure-

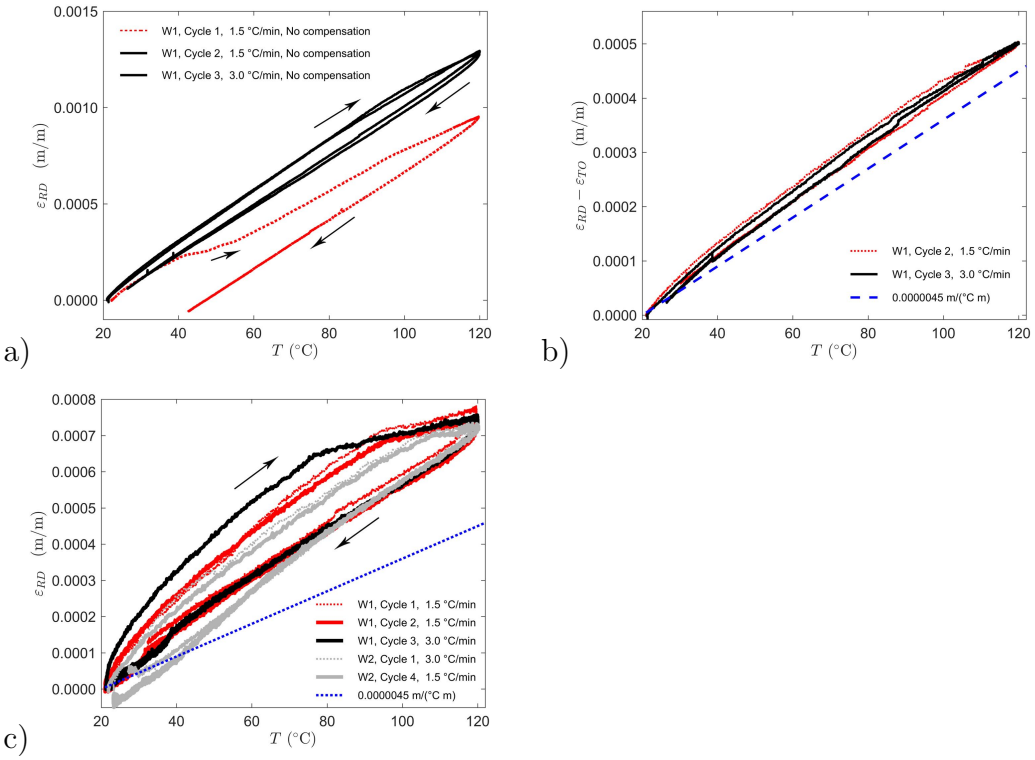

Figure 6: Temperature cycling for calibration: a) raw data from FBG sensors for different cure cycles; b) temperature-compensated data from FBG sensors for a typical cure cycle; c) raw data from strain gauges for different cure cycles.

ments incur significantly higher error (non-linearity) due to heat conducted via lead wires and presumably due to stronger effect by the bonding over a large sensor base. The ε-T slope during the heating experiences a sudden turn at high temperatures—due to reaching T_g and relaxation of the bonding epoxy. Also, the temperature measured by the Pt-100 sensor upon the heat-up does not exactly match the tungsten foil and gauge temperature. The effect by the heating rate applied per cycle can clearly be observed since it shifts the slope turning point towards the determined T_g = 116.9 ℃ (DSC). An apparent CTE as high as 6.620 ± 0.178 µm/(m ℃) was determined based on all the raw data. According to the known CTE of tungsten, linear correction functions for the strain gauges were determined: $Cr(T)$ = -2.238 µm/(m ℃) ($T - T_0$) and $Cr(T)$ = -2.207 µm/(m ℃) ($T - T_0$) for every first cycle after gauge bonding, and for further cycles, respectively.

3.3. Measured thermal expansion of UD CFRP laminate

In order to determine the effect of sensor embedding on the signal output and also to gain material data for the simulation, thermal expansion behavior of the CFRP was measured. Raw and error-corrected data from the temperature cycling of the fully cured CFRP sample is shown in Fig. 7. It can be seen that the strain indicated by an FBG sensor is mostly due to thermal effects by the optical fiber itself (5...8 µm/(m ℃)[33]), which emphasizes the difficulty in determining the CTE of CFRP and CFRP-based hybrids. After temperature compensation and error-correction, CTE for the linear region of the cool-down phase ($T = 110 \pm 1$ ℃...54 ± 21 ℃) was determined. Based on the FBG sensor data, fiber-direction CTE of -0.952 ± 0.021 µm/(m ℃) was determined—essentially agreeing typical values of comparable CFRP UD laminates [13, 34]. For the strain gauge output, the error-corrected data was far from a straight line, yet a fit over the linear region of the cool-down phase resulted in a reasonable CTE estimate of -0.857 ± 0.129 µm/(m ℃)—the deviation covering the average CTE value determined using the FBG sensor data.

For the transverse direction, only strain gauge data was measured. The response was merely linear up to the glass transition onset (85–95 ℃). Above the proportionality limit, the strain accumulation increased, suggesting rather strong Poisson's effect due to the contraction in the CFRP fiber direction. The non-linear behavior could also be due to gauge debonding—however, the cool-down curves matched with the heat-up curves indicating good bond. Least squares fitting over the linear region ($T = 111 \pm 2$ ℃...66 ± 1 ℃) resulted in a CTE estimate of 43.85 ± 0.87 µm/(m ℃)—which agrees well with the simulation results and experimental data of comparable CFRP materials in the current literature [35, 36].

3.4. Correction function for embedded strain gauges

The measurements reported in Sections 3.2 and 3.3 were acquired by using sensors bonded on a free surface. If measurements are to be made using fully embedded sensors, the effects due to the embedding must be known. To determine correction functions for embedding, CFRP samples were cured inside the silicone mould (see Fig. 2) with sensors placed between the prepreg layers during fabrication; a symmetric lay-up of $[0_{10}/S/0_{10}]$ was applied. Raw data from an embedded strain gauge is shown in Fig. 8(a). During the heat-up within the first cure cycle, the gauge is essentially free to expand itself (adoptable CTE 1.0 µm/(m ℃)) as well as along the expanding matrix

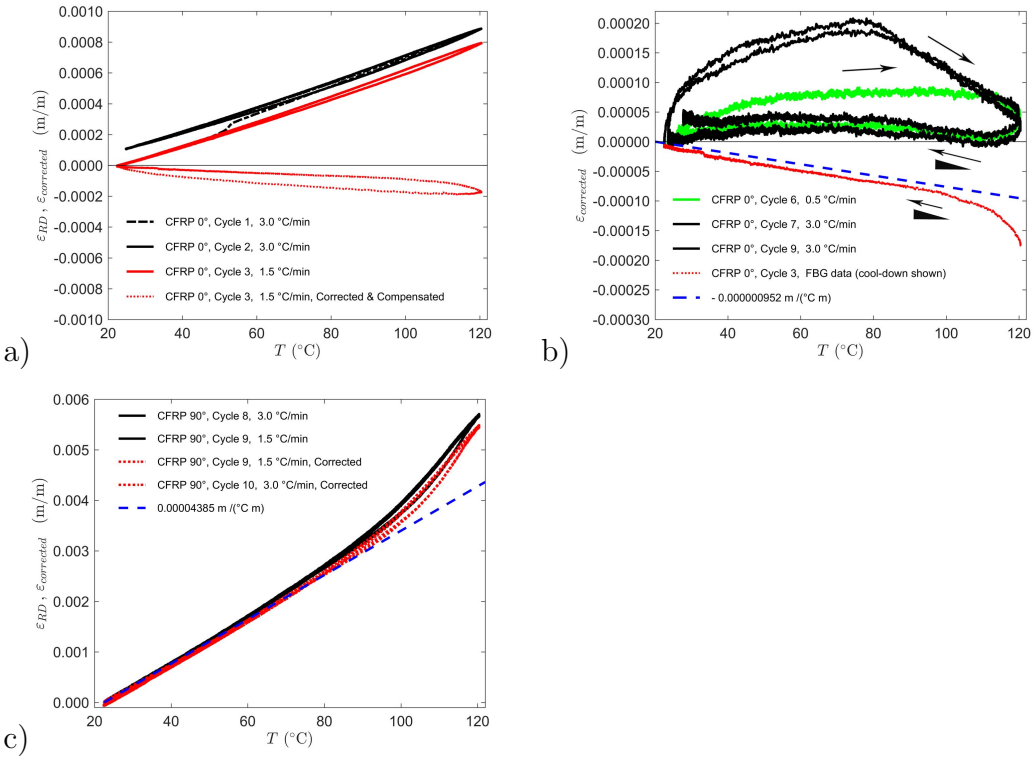

Figure 7: Temperature cycling for fully cured CFRP: a) raw data in (UD) fiber direction from FBG sensors; b) temperature-compensated and error-corrected data in (UD) fiber direction from strain gauges and a FBG sensor; c) raw data, error-corrected, and fitted ε-T curves in transverse direction based on strain gauge data.

resin of the pre-preg. In turn, during the cool-down phase, the gauge bonds to the cured CFRP—the following response being essentially linear. Again, the non-linearity during the heat-up is strongly heating rate-dependent and theoretically could be minimized using as low as possible heating rate. A comparison with the data using a fully cured CFRP and surface mounting are given in Fig. 8(b). The correction function for the embedding placement was determined for raw data to avoid error due to the linearization of the error-correction function (determined in Section 3.2). For simplification, the embedding correction function was defined linear (see Eq. 2), with a final form of $Cr_e(T) = 1.60$ µm/(m ℃) $(T - T_0)$. The FBG sensors did not experience identifiable error due to the embedding. FBG sensors are in general used as embedded and behave well in composite material applications [15, 13].

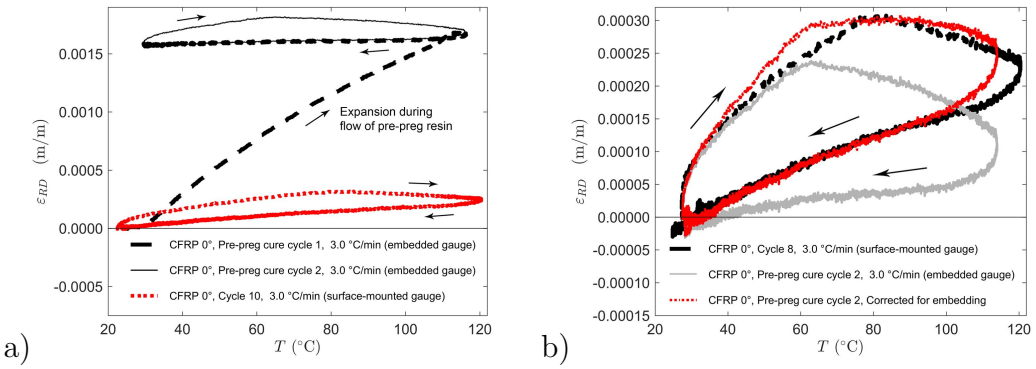

Figure 8: Temperature cycling on CFRP with embedded sensors: a) raw data in (UD) fiber direction from strain gauges for a typical cure cycle; b) comparison of raw data in (UD) fiber direction for an embedded strain gauge and free surface-mounted strain gauge.

3.5. Internal strains in CFRP-W hybrids

The thermo-mechanical response of the CFRP-tungsten hybrids in the fiber direction was analyzed using sensors bonded on tungsten foil using the bonding epoxy. Prior to lamination, the sensor bond was post-cured using a typical cure cycle (see Fig. 1) to avoid non-linearity due to yielding of the bonding epoxy. Test samples were prepared (1) with an FBG sensor and strain gauge bonded side-by-side, (2) with a strain gauge alone, and also (3) without any sensor mounting. Typical raw data measured using a strain gauge is shown in Fig. 9(a). The tungsten foil expands rather freely during the first cycle, resembling measurements shown in Fig. 6(c). During the cool-down phase, the tungsten layer with the sensors bonds to the cured CFRP—the response being essentially linear. Fig. 9(b) shows temperature-compensated and error-corrected data from an FBG sensor and the same hybrid sample as in Fig. 9(a)—indicating the negative effective CTE of the hybrid sample in the fiber direction (slope during the cool-down). Fitting over the linear region ($T = 110 \pm 3$ ℃...65 ± 3 ℃) of the cool-down phase resulted in CTE estimates of -0.497 ± 0.001 µm/(m ℃) and -0.630 ± 0.083 µm/(m ℃) for the FBG data and strain gauge data, respectively, when data from a single sample with both sensors is used. The variation between different hybrid samples was studied using strain gauge measurements; the variation in the effective CTE was observed high (0.617 ± 1.297 µm/(m ℃)) as is reported typical of metal-polymer hybrids in the current literature [36, 22].

The FBG data measured using a fully cured hybrid sample completely

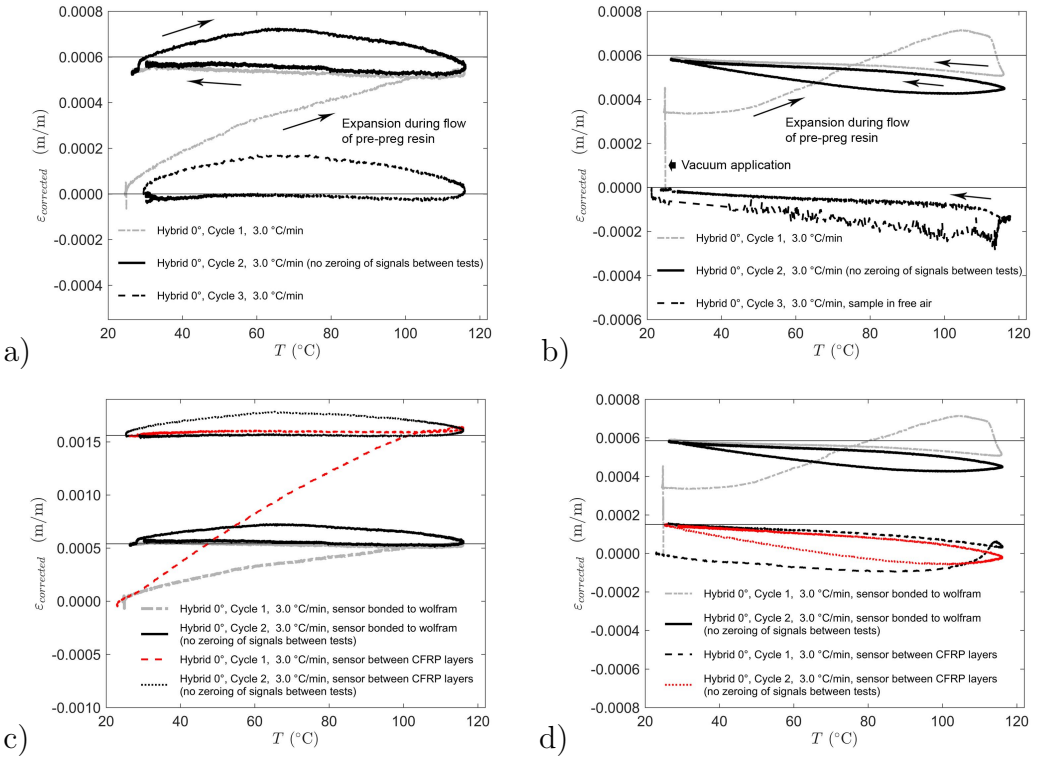

Figure 9: Temperature cycling on CFRP-tungsten hybrids: a) raw data in (UD) fiber direction from a strain gauge; b) temperature-compensated and error-corrected data in (UD) fiber direction from an FBG sensor; c) comparison of strain gauge data measured on tungsten and between CFRP layers; d) comparison of FBG sensor data measured on tungsten and between CFRP layers inside the hybrid.

removed from the mould and placed directly in oven air, illustrates the effect of the vacuum and the silicone mould (see Fig. 9(b)). The soft mould does not affect the thermal expansion (contraction) of the hybrid sample but the lack of vacuum condition increases non-linearity (mismatch with Pt-100) and the temperature compensation sensor records strains in the compensation FBG due to the fluctuation of the air circulating in the oven. Additionally, a comparison was made using sensors embedded between pre-preg layers (lay-up $[0_{14}/W/0/S/0_6]$) and not pre-bonded. There was no observable difference in the behavior during the cool-down phase (Figs. 9(c)–(d)).

The sensor bond and attachment to the surrounding CFRP material was studied via SEM imaging. For an optical fiber, the bonding on a free surface

basically encloses the grating (FBG), as shown in Fig. 10(a). In contrast, a strain gauge bonds from under the base and its sides with the bonding epoxy (see Fig. 10(b)), explaining the difference between surface-bonded and embedded mounting (see Section 3.4). Also, the embedding presumably inhibits heat conduction by the lead wires into the gauge grid.

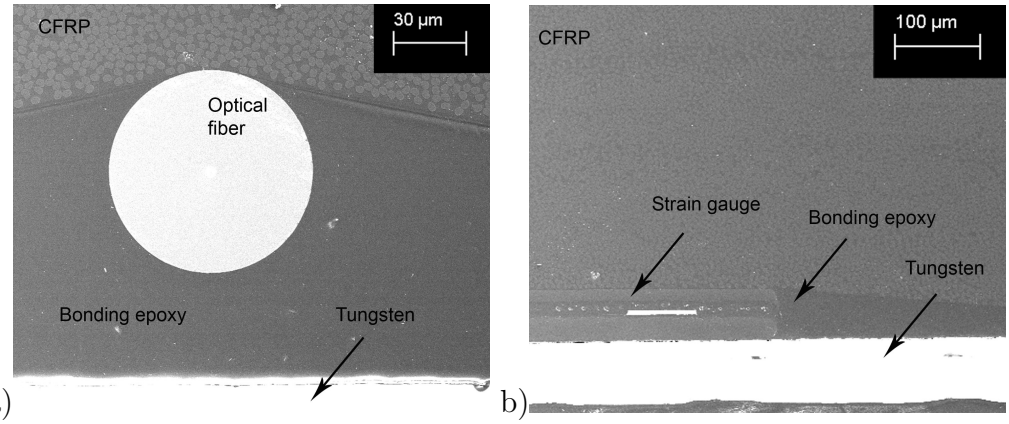

Figure 10: Cross-sectional SEM imaging of embedded sensors (hybrid sample): a) FBG sensor; b) strain gauge.

3.6. Curvature due to residual stresses and mould deformation

The anisotropic material properties and the asymmetric lay-up of the hybrid samples results in deformation within the cure cycle. However, the deformations are very slight and accompanied by curvature due to deformation of the silicone mould by the vacuum bag. The overall shape of a pure CFRP sample was measured to determine the effect of mould deformation, as shown in Fig. 11(a). To determine curvatures of the hybrid samples, local measurements were used (Fig. 11(b)). It can be seen (Fig. 11(c)) that, due to the deformation of the mould, the pure CFRP samples are thicker in the middle (curvature for the longitudinal direction 219.1 mm). Also, it can be seen that the roughness introduced by the peel ply fabric was within the order of magnitude of the deformation by residual strains (i.e. curvature). The curvature of the hybrid samples was generally low, compared to the transverse direction, and seemed not to represent an ideal circle. Least squares fitting resulted in estimative radiuses of curvature (series of five samples) of 501.4 $\pm$ 220 mm and 128.6 $\pm$ 32 mm for the fiber and transverse direction, respectively.

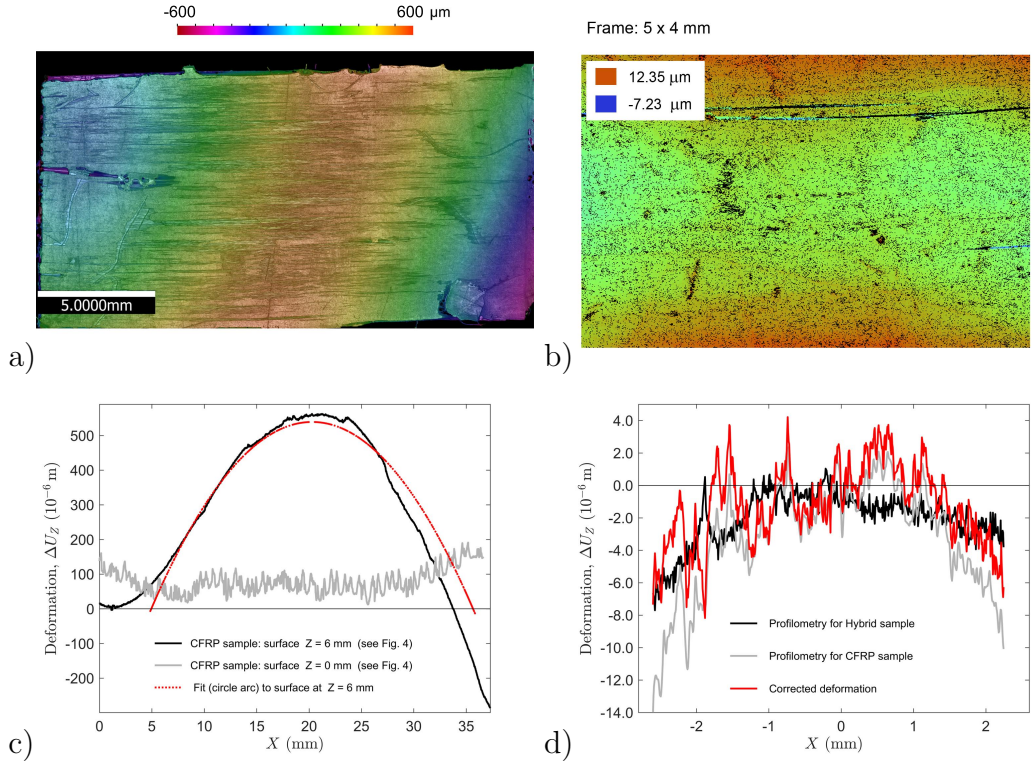

Figure 11: Measured surface shapes: a) overall scan on pure CFRP sample ($Z = 6$ mm); b) local scan on CFRP-tungsten hybrid ($Z = 6$ mm); c) top and bottom surface curvature on pure CFRP sample; d) local surface curvature on CFRP-tungsten hybrid ($Z = 6$ mm) with compensation based on CFRP sample shape (measurement origin shifted to $X = 19.5$ mm).

3.7. Simulated deformation and internal strains

FEA can be used to compute the accumulation of pure residual strain without any influence of sensors in the CFRP-tungsten hybrid during a virtual cool-down phase. The macro-scale deformation according to the simulation is shown in Fig. 12, illustrating the double-curved shape observed from the profilometer data correspondingly. The longitudinal curvature by the simulation is significantly less (radius 460 m) than what was fitted based on the profilometry and compensated using the pure CFRP sample's curvature (resulting radius 282 mm). Here, the deformation of the very stiff hybrid sample due to the asymmetric lay-up is simply within the surface roughness and mould-deformation of the experiments making the comparison based on deformations difficult. The experimental and simulated strain buildup on the

surface of the tungsten layer is presented in Fig. 13(a)–(b). Over the sensor location (≈5 mm away from free edge), the longitudinal strain is essentially constant, ruling out the effect of strain gradient on the experimentally measured strains. As a function of temperature difference, the absolute residual strain builds up higher in the simulation over the linear range. The results show that the CTE value determined for the CFRP parts is crucial for the accuracy of the residual strain simulation in hybrid materials. This underlines the fact that direct measurement of residual strain in each specific structural part is important. It is well known that the thermal expansion of CFRP is extremely sensitive to slight changes, e.g., in the fiber volume fraction [36], and results considerably scatter between different items.

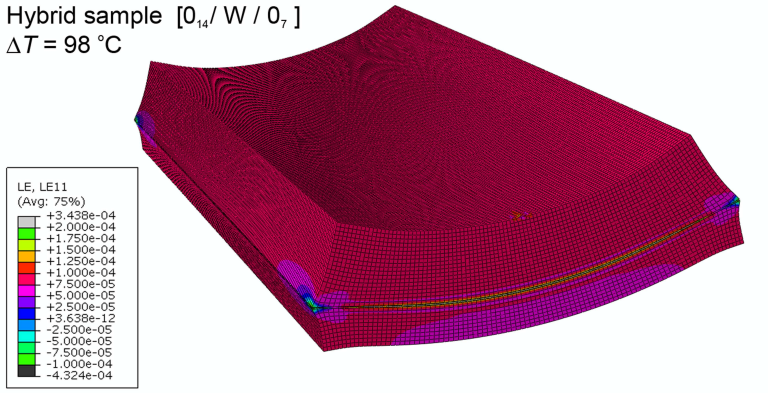

Figure 12: Finite element analysis of the thermo-mechanical response: simulated overall deformation and longitudinal strain (LE11 = ε_{xx}) in the hybrid sample. The deformation scale is ×80 in the figure and data was recorded for a thermal load of $\Delta T = 98$ °C.

4. Conclusions

Embedded foil strain gauges has not been successfully applied for measuring thermal expansion (residual strain) in CFRP and no attempt has been published using hybrid materials in the current literature. In this work, the application of structure-integrated strain gauges was studied for hybrid laminates, which were prepared using CFRP and tungsten foils and intended for spacecraft applications. Test-specific correction functions for thermal output were first calibrated based on thermal expansion of pure tungsten. Second, the effect of sensor embedding into CFRP was determined for the strain

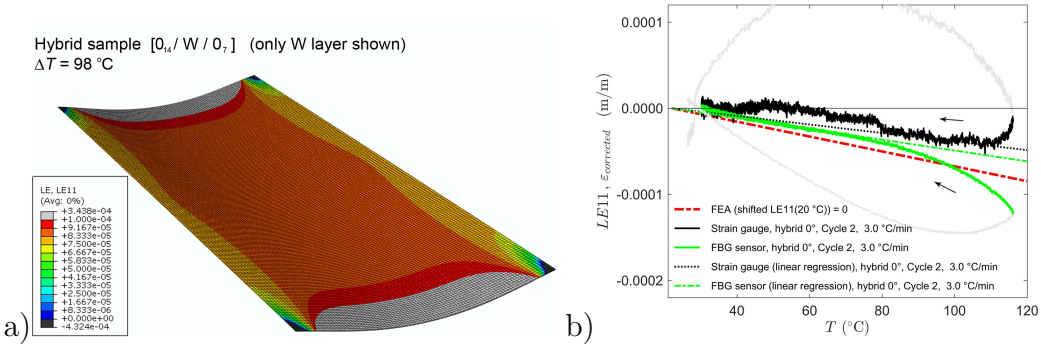

Figure 13: Comparison of the experimental data and simulated longitudinal strain (LE11 $= \varepsilon_{xx}$) during the cool-down phase: a) simulated distribution over the tungsten layer inside the hybrid; b) strain buildup as a function of temperature. The FEA deformation scale is $\times 80$ in the figure.

measurements. Third, the strain accumulation in the CFRP-tungsten hybrid during different cure cycles was analyzed based on the data from strain gauges, fiber Bragg grating sensors, and a finite element simulation. The main conclusions based on the results are:

- Embedded electrical resistance strain gauges can be used to determine thermal expansion of a hybrid laminate with a high accuracy when thermal output is compensated using a case-specific correction function (absolute residual strain error < 75 µm/m in this study).

- The correction function for an embedded strain gauge must account for the specific temperature measurement setup, gauge bonding, and embedding.

- When compared to measurements using fiber Bragg grating sensors, the relative difference for the strain gauge data is on a reasonable level (difference in the linearized CTE of the hybrid $\approx$20%).

- For accurate residual strain measurements during temperature cycling, the underlining cause of varying error in the determined mechanical strain is the mismatch between the prevailing temperature in the strain sensor and the prevailing temperature in the temperature sensor. An independent temperature sensor should be positioned as close as possible to the strain sensor and with minimum effects to strain fields.

5. Acknowledgement

This investigation was partly funded by a grant from the Finnish Metals and Engineering Competence Cluster and partly by a grant from the European Communitys Seventh Framework Programme (FP7/2007-2013) under Grant Agreement 262746. P. Antunes also acknowledge the financial support from the Portuguese national funding agency for science (FCT) through the fellowship SFRH/BPD/76735/2011. The authors want to thank researchers M. Laulajainen, T. Pärnänen, K. Rämö and A. Tauriainen for their assistance. Synoste Ltd (Finland) and Straintech Finland Ltd are acknowledged for their collaboration.

References

[1] Li, C., Potter, K., Wisnom, M., Stringer, G.. In-situ measurement of chemical shrinkage of MY750 epoxy resin by a novel gravimetric method. Compos Sci Technol 2004;4(1):55–64.

[2] Yu, Y., Ashcroft, I., Swallowe, G.. An experimental investigation of residual stresses in an epoxy-steel laminate. Int J Adhes Adhes 2006;26(7):511–519.

[3] Kinloch, A., Thrusabanjong, E., Williams, J.. Fracture at bimaterial interfaces: the role of residual stresses. J Mater Sci 1991;26(23):6260–6270.

[4] Pärnänen, T., Alderliesten, R., Rans, C., Brander, T., Saarela, O.. Applicability of AZ31B-H24 magnesium in fibre metal laminates - an experimental impact research. Compos Part A Appl Sci Manuf 2012;43(9):1578–1586.

[5] Talagani, M., DorMohammadi, S., Dutton, R., Godines, C., Baid, H., Abdi, F., et al. Numerical simulation of big area additive manufacturing (3D printing) of a full size car. Sampe J 2015;51(4):27–36.

[6] Nairn, J.. Fracture mechanics of composites with residual thermal stresses. J App Mech, Transactions ASME 1997;64(4):804–810.

[7] Jumbo, F., Ashcroft, I., Crocombe, A., Abdel Wahab, M.. Thermal residual stress analysis of epoxy bi-material laminates and bonded joints. Int J Adhes Adhes 2010;30(7):523–538.

[8] Rosso, P., Váradi, K.. FE macro/micro analysis of thermal residual stresses and failure behaviour under transverse tensile load of VE/CF - fibre bundle composites. Compos Sci Technol 2006;66(16):3241–3253.

[9] Yokozeki, T.. Energy release rates of bi-material interface crack including residual thermal stresses: Application of crack tip element method. Eng Fract Mech 2010;77(1):84–93.

[10] Zhang, J., Soutis, C., Fan, J.. Effects of matrix cracking and hygrothermal stresses on the strain energy release rate for edge delamination in composite laminates. Composites 1994;25(1):27–35.

[11] Rans, C., Alderliesten, R., Benedictus, R.. Misinterpreting the results: How similitude can improve our understanding of fatigue delamination growth. Compos Sci Technol 2011;71(2):230–238.

[12] Colpo, F., Humbert, L., Botsis, J.. Characterisation of residual stresses in a single fibre composite with FBG sensor. Compos Sci Technol 2007;67(1):1830–1841.

[13] Kim, H.S., Yoo, S.H., Chang, S.H.. In situ monitoring of the strain evolution and curing reaction of composite laminates to reduce the thermal residual stress using FBG sensor and dielectrometry. Compos Part B Eng 2013;44(1):446–452.

[14] Okabe, Y., Yashiro, S., Tsuji, R., Mizutani, T., Takeda, N.. Effect of thermal residual stress on the reflection spectrum from fiber Bragg grating sensor embedded in CFRP laminates. Compos Part A Appl Sci Manuf 2002;33(7):991–999.

[15] Vohra, S.. Handbook of optical fibre sensing technology; chap. Optical fiber gratings applications. Wiley, Chichester, UK; 2002, p. 476–504.

[16] Sierra-Pérez, J., Torres-Arredondo, M., Güemes, A.. Damage and nonlinearities detection in wind turbine blades based on strain field pattern recognition. FBGs, OBR and strain gauges comparison. Compos Struct 2016;135(1):156–166.

[17] Du, W., Tao, X., Tam, H., Choy, C.. Fundamentals and applications of optical fiber bragg grating sensors to textile structural composites. Compos Struct 1998;42(3):217–229.

[18] Friebele, E., Askins, C., Bosse, A., Kersey, A., Patrick, H., Pogue, W., et al. Optical fiber sensors for spacecraft applications. J Smart Mat Struct 1999;8(6):813.

[19] Murray, W., Miller, W.. The bonded electrical resistance strain gage: an introduction; chap. Temperature effects on strain gages. Oxford University Press, US; 1992, p. 337–359.

[20] Lanza di Scalea, F.. Measurement of thermal expansion coefficients of composites using strain gages. Exp Mech 1998;38(4):233–241.

[21] Mulle, M., Zitoune, R., Collombet, F., Olivier, P., Grunvald, Y.. Thermal expansion of carbon-epoxy laminates measured with embedded FBGS - Comparison with other experimental techniques and numerical simulation. Compos Part A Appl Sci Manuf 2007;38(1):1414–1424.

[22] Kanerva, M., Saarela, O.. X-ray diffraction and fracture based analysis of residual stresses in stainless steel-epoxy interfaces with electropolishing and acid etching substrate treatments. Int J Adhes Adhes 2012;39:60–67.

[23] Lunt, A., Korsunsky, A.. A review of micro-scale focused ion beam milling and digital image correlation analysis for residual stress evaluation and error estimation. Surf Coat Technol 2015;283:373–388.

[24] Sanderson, T.. On the evaluation of residual stresses in bi-layer materials using the bent strip method. Surf Coat Technol 2008;202(8):1493–1501.

[25] Curiel, T., Fernlund, G.. Deformation and stress build-up in bi-material beam specimens with a curing FM300 adhesive interlayer. Compos Part A Appl Sci Manuf 2008;39(2):252–261.

[26] Shokrieh, M., Daneshvar, A., Akbari, S.. Reduction of thermal residual stresses of laminated polymer composites by addition of carbon nanotubes. Mater Des 2014;53:209–216.

[27] Kanerva, M., Sarlin, E., Hållbro, A., Jokinen, J.. Plastic deformation of powder metallurgy tungsten alloy foils for satellite enclosures. In: 30^{th} Congress of the International Council of the Aeronautical Sciences ICAS (Proceedings). Daejeon, South Korea; 2016,September 23-30.

[28] Method of compensating temperature effect of lead wire. Kyowa Electronic Instruments Co., Ltd; August, 2016 (cited). http://www.kyowa-ei.com/eng/technical/notes/ technical note/3 wire_system.html/.

[29] Kanerva, M., Jokinen, J., Antunes, P., Wallin, M., Brander, T., Saarela, O.. Acceptance testing of tungsten-CFRP laminate interfaces for satellite enclosures. In: 20^{th} International Conference on Composite Materials (Proceedings). Copenhagen, Denmark; 2015,July 19-24.

[30] Zhang, X., Yan, Q., Yang, C., Wang, T., Ge, C.. Microstructure, mechanical properties and bonding characteristic of deformed tungsten. Int J Refractory Met Hard Mat 2014;43(1):302–308.

[31] Araldite LY 5052 / Aradur 5052 cold curing epoxy systems. Technical Data Sheet, Huntsman; 2010.

[32] ACG MTM 57 series prepreg system. Advanced Composites Group Ltd.; 2009. Product Description PDS1075/01.10/7.

[33] Kreuzer, M.. Strain measurements with fiber bragg grating sensors. Tech. Rep.; HBM GmbH, Darmstadt, Germany; 2016 (cited).

[34] M40J Data Sheet, CFA-014. Toray Carbon Fibers America, Inc., USA; August, 2016 (cited). http://www.toraycfa.com/pdfs/M40JDataSheet.pdf/.

[35] Sideridis, E.. Thermal expansion coefficient of fiber composites defined by the concept of the interphase. Compos Sci Technol 1994;51(1):301–317.

[36] Karadeniz, H., Kumlutas, D.. A numerical study on the coefficients of thermal expansion of fiber reinforced composite materials. Compos Struct 2007;78(1):1–10.

[37] Principle of self-temperature-compensation gauges (SELCOM gauges). Kyowa Electronic Instruments Co., Ltd; August, 2016 (cited). http://www.kyowa-ei.com/eng/technical/notes/ technical_note/selcom_gages.html/.

Appendix A.

Appendix A.1. Error sources of electrical resistance foil strain gauges

In general, the strain reading from any instrumented sample is determined based on the resistance change (ΔR) in the strain gauge grid:

$$\varepsilon_{RD} = \frac{\Delta R}{G_s}, \tag{A.1}$$

where G_s is the gauge factor of the strain gauge grid. However, due to a change in temperature during a measurement, the strain gauge reading will indicate the following combination:

$$\varepsilon_{RD} = \varepsilon_{MD} + \varepsilon_{TO} + \varepsilon_{W}, \tag{A.2}$$

where ε_{MD} is the strain in the measured sample material due to external mechanical loading, ε_{TO} is the thermal output (i.e. strain due to thermal effects, sometimes called 'apparent strain'), and ε_W is false strain indication due to thermally induced resistance changes in the lead wires of the gauge.

The strain due to thermal effects (ε_{TO}) is governed by the following generalized equation [19]:

$$\varepsilon_{TO} = \left[\frac{\alpha_R(T)}{G_s} + \frac{1 + K_t(\alpha_m + \alpha_{gb} + \alpha_g}{1 - K_t \mu_c} \right] \Delta T, \tag{A.3}$$

where ΔT is the prevailing temperature difference, $\alpha_R(T)$ is the resistive temperature coefficient of the strain gauge as a function of temperature, α_g is the coefficient of linear thermal expansion (CTE) of the gauge grid, α_m is the CTE of the measured sample material, α_{gb} is the CTE of the gauge base, K_t is the transverse sensitivity factor of the strain gauge, and μ_c is the Poisson's ratio of the material used in the gauge calibration (by the manufacturer). It is clear that the strain reading due to thermal effects can be totally cancelled, when the right-hand side in Eq. A.3 yields zero. Eq. A.3 is usually presented in a simplified form [37]:

$$\varepsilon_{TO} = \left[\frac{\alpha_R(T)}{G_s} + (\alpha_m - \beta_g) \right] \Delta T, \tag{A.4}$$

where β_g is the 'adoptable' CTE of the strain gauge (combination of base and grid properties).

In addition to the thermal effects defined above, the strain-to-electric resistance relation of the grid material (Eq. A.1) does not remain constant due to change of temperature. Therefore, the value of the gauge factor is typically corrected as follows [19]:

$$G_{sT} = G_{sR}\left[1 + \frac{\Delta G_F(\%)}{100}\right]\Delta T, \tag{A.5}$$

where G_{sT} is the gauge factor at a specific 'ambient' temperature, G_{sR} is the gauge factor at a reference temperature, and G_F is the percentage change in the gauge factor when the temperature shifts from the ambient temperature to the reference (test) temperature.

Appendix A.2. Thermal compensation of FBG sensors in optical fibers

In an optical fiber, the grating periodicity (grid spacing) of an FBG sensor, G_{FBG}, determines the specific wave-length (peak) of the reflected light [15]:

$$G_{FBG} = \frac{\lambda_B}{2n}, \tag{A.6}$$

where λ_B is the Bragg wave-length and n is the effective refractive index (1.45) of the optical fiber core. Any change in the grid spacing, or in the refractive index, will lead to a shift in the reflected wave-length peak, and can be transformed to a strain reading:

$$\frac{\Delta\lambda}{\lambda_B} = k \cdot \varepsilon_{RD}, \tag{A.7}$$

where the factor k is based on the photo-elastic coefficient, p, of the optical fiber ($k = 1 - p \approx 0.78$ [15]).

In the event of temperature change during a test, the fiber will expand (affecting grid spacing) and the refractive index will alter as well. These thermal effects can be compensated from the strain indication as follows [33]:

$$\varepsilon_{RD} - \varepsilon_{TO} = \frac{\Delta\lambda}{\lambda_B}\frac{1}{k} - \left(\alpha_{gr} + \frac{\alpha_\delta}{k}\right)\Delta T, \tag{A.8}$$

where ΔT is the prevailing temperature difference, α_{gr} is the CTE of glass (silica), α_δ is the thermo-optic coefficient.